NANO · MICRO small
www.small-journal.com

Remarkable Improvement in Photocatalytic Performance for Tannery Wastewater Processing via SnS_2 Modified with N-Doped Carbon Quantum Dots: Synthesis, Characterization, and 4-Nitrophenol-Aided Cr(VI) Photoreduction

*Shuo Wang, Liping Li, Zhenghui Zhu, Minglei Zhao, Liming Zhang, Nannan Zhang, Qiannan Wu, Xiyang Wang, and Guangshe Li**

Photocatalytic pathways are proved crucial for the sustainable production of chemicals and fuels required for a pollution-free planet. Electron–hole recombination is a critical problem that has, so far, limited the efficiency of the most promising photocatalytic materials. Here, the efficacy of the 0D N doped carbon quantum dots (N-CQDs) is demonstrated in accelerating the charge separation and transfer and thereby boosting the activity of a narrow-bandgap SnS_2 photocatalytic system. N-CQDs are in situ loaded onto SnS_2 nanosheets in forming N-CQDs/SnS_2 composite via an electrostatic interaction under hydrothermal conditions. Cr(VI) photoreduction rate of N-CQDs/SnS_2 is highly enhanced by engineering the loading contents of N-CQDs, in which the optimal N-CQDs/SnS_2 with 40 mol% N-CQDs exhibits a remarkable Cr(VI) photoreduction rate of 0.148 min^{-1}, about 5-time and 148-time higher than that of SnS_2 and N-CQDs, respectively. Examining the photoexcited charges via zeta potential, X-ray photoelectron spectroscopy (XPS), surface photovoltage, and electrochemical impedance spectra indicate that the improved Cr(VI) photodegradation rate is linked to the strong electrostatic attraction between N-CQDs and SnS_2 nanosheets in composite, which favors efficient carrier utilization. To further boost the carrier utilization, 4-nitrophenol is introduced in this photocatalytic system and the efficiency of Cr(VI) photoreduction is further promoted.

1. Introduction

With a sharp increase in demand for leather products around the world,[1] more and more tannery wastewater is poured into natural water. Two industrial wastes come out as a threat to human health, which are dichromate used during tanning process and 4-nitrophenol (4-NP) used for antimildew process, respectively.[2] To address the growing environmental concerns, several strategies have been developed to dispose tannery wastewater, among which photocatalysis appears to offer a "green" approach with a lot of merits as demonstrated in applications such as water splitting,[3] carbon dioxide reduction,[4] nitrogen fixation,[5] and most importantly, complete elimination of toxic organic pollutants and heavy metal ions in environmental remediation.[6] Even so, most photocatalysts are wide bandgap semiconductors, which could be excited only by ultraviolet region of solar spectrum, leaving 95% energy of total solar spectrum wasted.[7] Alternatively, many metal sulfide semiconductors have been reported to act as visible-light-driven photocatalysts, since these metal sulfide semiconductors have bandgap energies matching well the visible range of solar spectrum.[8] As a result, metal sulfide semiconductors (such as $AgSbS_2$,[9] In_2S_3,[10] CdS,[11] $CuInS_2$,[12] PbS.[13]) have been studied for degrading and reducing toxic substances. Despite of some progress, parts of metal sulfide semiconductors still contain toxic or expensive elements, which may cause secondary pollution to the environment, or demerits for sustainable applications.

Tin disulfide (SnS_2) is a promising photocatalyst owing to its low toxicity, economic cost, and wide spectral response, favoring the concept of green chemistry.[14] However, limited by separating and transferring of photogenerated charges, SnS_2 possesses a low photocatalytic efficiency.[14,15] Although loading noble metals as cocatalysts is an effective way to improve electron–hole separation, corresponding cost is highly increased.[16] In this case, developing low cost cocatalyst with non-noble metal is highly demanding.

S. Wang, Prof. L. Li, Z. Zhu, N. Zhang, X. Wang, Prof. G. Li
State Key Laboratory of Inorganic Synthesis and Preparative Chemistry
College of Chemistry
Jilin University
Changchun 130026, P. R. China
E-mail: guangshe@jlu.edu.cn
Dr. M. Zhao
New York University College of Dentistry
New York, NY 10010, USA
Dr. L. Zhang
State Key Laboratory of Luminescence and Applications
Changchun Institute of Optics Fine Mechanics and Physics
Chinese Academy of Sciences
Changchun 130033, P. R. China
Q. Wu
College of Chemistry
Jilin University
Changchun 130012, P. R. China
The ORCID identification number(s) for the author(s) of this article can be found under https://doi.org/10.1002/smll.201804515.

DOI: 10.1002/smll.201804515

Carbon quantum dots (CQDs) may help to achieve this goal, since CQDs are featured by many excellent size-dependent properties,[17] and since CQDs belong to a kind of carbon material with particle size less than 10 nm, which consisted of sp^2/sp^3 hybridized carbon atoms.[18] CQDs have merits of chemical inertness, excellent biocompatibility, low cytotoxicity, and low cost.[19] One has witnessed many potential applications of CQDs in bioimaging,[20] drug delivery,[20] storage materials,[21] luminescence,[22] and photocatalysis.[23] Doping in CQDs can effectively improve optical and electrical properties,[24,25] especially narrow bandgap,[24] to harvest a broader range of visible or near-infrared light and increase electron mobility. These virtues make doped CQDs as the promising metal-free cocatalyst candidates to separate and transfer the photogenerated charges of SnS_2 more efficiently.

In this work, N_{23}-CQDs are synthesized and loaded onto SnS_2 nanosheets by an in situ hydrothermal method. Both N doping amounts in N_{23}-CQDs and N_{23}-CQDs loading contents on SnS_2 nanosheets were optimized to achieve an effective Cr(VI) photoreduction. The kinetic analysis together with the surface photovoltage (SPV) response and electrochemical impedance spectra (EIS) demonstrated a dramatic enhancement in the separation of photogenerated electrons and holes for N_{23}-CQDs. N_{23}-CQDs loading content dependent photocatalytic properties were also investigated in detail. It is found that N_{23}-CQDs played a key role in significantly accelerating the separation of photogenerated electrons and holes. Furthermore, deliberately introducing 4-NP as hole-acceptor could further accelerate the separation and utilization of photogenerated electrons and holes as well.

2. Results and Discussion

2.1. In Situ Formation of N_{23}-CQDs/SnS_2

The synthesis of 40 mol% N_{23}-CQDs/SnS_2 is based on a controllable in situ loading approach, which initially produces N_{23}-CQDs that are then loaded on SnS_2 nanosheets via an electrostatic interaction by hydrothermal conditions. The nature of the charges on the surface of N_{23}-CQDs and SnS_2 favors the attraction of both components, which could be evidenced by the values of zeta potential. The zeta potential value of pristine SnS_2 nanosheets is +4.31 mV when SnS_2 nanosheets were dispersed in distilled water, while the zeta potential of N_{23}-CQDs is −9.44 mV. This result means that the surfaces of SnS_2 and N_{23}-CQDs possess the opposite charges. More negative zeta potential the material has, the richer negative charge is on its surface, and vice versa.[26] However, the zeta potential for 40 mol% N_{23}-CQDs/SnS_2 is −4.55 mV, which is in between those of N_{23}-CQDs and SnS_2. Data analyses showed that there are plenty of negative functional groups such as carboxyl ($-COO^-$) on the surface of N_{23}-CQDs, which could notably offset the positive charge on the surface of SnS_2.[27] Therefore, in situ loading could spontaneously occur to form N_{23}-CQDs/SnS_2 due to the strong electrostatic interactions between N_{23}-CQDs and SnS_2 nanosheets. We simulated the combination of SnS2 and N:CQDs, as depicted in **Figure 1**j. The in situ loading N_{23}-CQDs on SnS_2 to successfully obtain N_{23}-CQDs/SnS_2 catalyst was further demonstrated by transmission electron microscopy and high-resolution TEM. Figure 1a–f shows the TEM and HRTEM images of the samples N_{23}-CQDs, SnS_2, and 40 mol% N_{23}-CQDs/SnS_2. 0D N_{23}-CQDs is about 2.7 nm in diameter, and the size distribution is limited in 2–3 nm (Figure 1g). The lattice spacing between two adjacent lattice fringes in Figure 1b is 0.32 nm, which could be indexed to plane (002) of graphitic carbon.[28] SnS_2 nanosheets and 40 mol% N_{23}-CQDs/SnS_2 catalyst showed uniform and distinct diameters from N_{23}-CQDs (see histograms associated with Figure 1a–f and Figure 1g–i). Both 40 mol% N_{23}-CQDs/SnS_2 and SnS_2 have the same sheet nanostructures, and the average diameter of these nanostructures is around 32 nm (Figure 1h,i). However, compared with SnS_2 nanosheets, 40 mol% N_{23}-CQDs/SnS_2 showed the overlapping and stacking features of the multiple nanosheets. Moreover, the lattice spacing between two adjacent lattice fringes in Figure 1d is 0.589 nm, which could be ascribed to plane (001) of SnS_2.[29] Both plane (001) of SnS_2 and plane (002) of N_{23}-CQDs were observed in 40 mol% N_{23}-CQDs/SnS_2, indicating that N_{23}-CQDs have been successfully formed and loaded on SnS_2 through in situ loading approach. Furthermore, the elemental mapping images of electron microscopy-energy dispersive X-ray spectroscopy (EM-EDS) in Figure S1 (Supporting Information) revealed that the elements C, N, Sn, and S are homogeneously distributed, which tentatively confirmed the formation of N_{23}-CQDs/SnS_2.

2.2. Surface Chemistry and Composition of N_{23}-CQDs/SnS_2 Loaded with Different Contents of N_{23}-CQDs

The surface chemistry, surface composition, and valence state of N_{23}.CQDs/SnS_2 loaded with different contents of N_{23}-CQDs were investigated by Fourier transform-infrared (FT-IR) spectroscopy, Raman, and XPS. **Figure 2** showed FT-IR spectra of N_{23}-CQDs/SnS_2 catalyst loaded with different contents of N_{23}-CQDs. The broad characteristic absorption band at 3400–3280 cm^{-1} is originated from O—H stretching vibration of the adsorbed H_2O molecules on the surface of N_{23}-CQDs/SnS_2.[30] Five absorptions at 3250–3050, 1638, 1580, and 1456–1325 cm^{-1} are characteristic of vibration bands for bonds N—H,[30,31] C=N,[32] N—H,[32] C—N, and N—H,[33,34] respectively. These could provide the powerful proof that the nitrogen atoms have been successfully incorporated into CQDs to form N_{23}-CQDs. Similar IR bands are well traced in IR bands of N_{23}.CQDs/SnS_2 with different N_{23}-CQDs loading contents, which indicates N_{23}-CQDs loading on SnS_2 nanosheets. Moreover, the stretching vibrations at 2924 and 2851, 1705, and 1157 cm^{-1} could be ascribed to the vibration bands of bonds C—H,[30,35] C=O,[31,36] and C—O,[31] which are closely associated with the carboxyl and other oxygen-containing functional groups on the surface of N_{23}-CQDs/SnS_2.[31] When comparing to FT-IR spectra of the pristine N_{23}-CQDs, the intensity of the stretching vibrations of these carboxyl and other oxygen-containing functional groups in 40 mol% N_{23}-CQDs/SnS_2 was dramatically decreased. This is mainly because when strongly interacting with the surface of SnS_2 to form N_{23}-CQDs/SnS_2, oxygen-containing functional groups became more relatively rigid than those free oxygen-containing functional groups in N_{23}-CQDs. These results further proved that N_{23}-CQDs/SnS_2 was constructed through the strong interaction between components N_{23}-CQDs and SnS_2. In addition, the vibrational peaks of

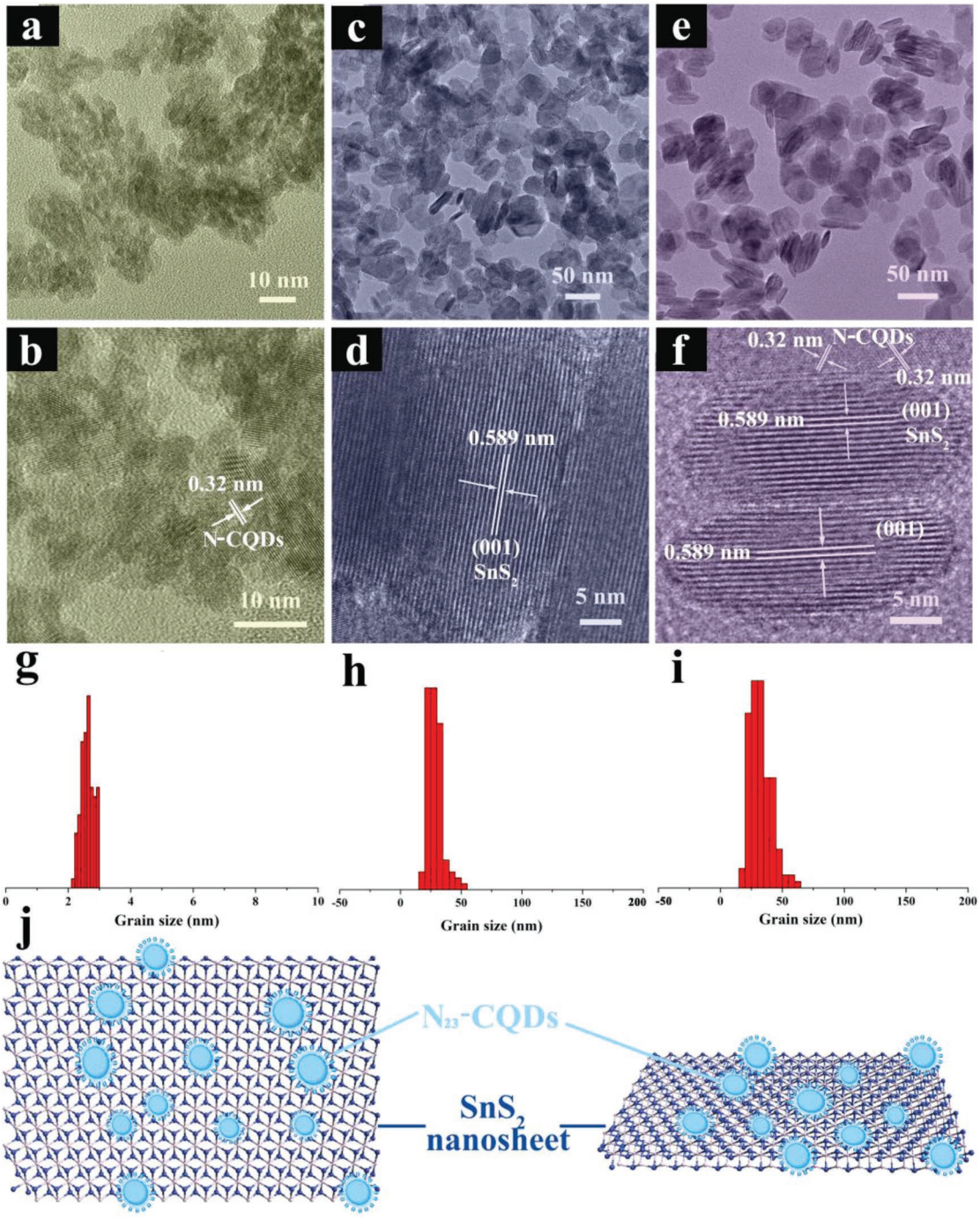

Figure 1. TEM and HRTEM images of a,b) N_{23}-CQDs, c,d) SnS_2, e,f) 40 mol% N_{23}-CQDs/SnS_2, and g–i) the corresponding particle size distributions. j) Schematic diagram of N_{23}-CQDs/SnS_2 configuration on top and side views: grey standards for Sn, dark blue for S, and light blue for N_{23}-CQDs with some oxygen-containing groups on surfaces.

SnS_2 remained around 500 cm^{-1} in FT-IR spectra of N_{23}-CQDs/SnS_2 regardless of N_{23}-CQDs loading content. Such characteristic bands are all traced from IR bands of N_{23}-CQDs/SnS_2 with different N_{23}-CQDs loading contents, which means that SnS_2 has preserved its lattice structure well after loading N_{23}-CQDs.

Analogously, Raman spectrum is another powerful tool to study surface chemistry of the samples. **Figure 3** showed Raman spectra of 40 mol% N_{23}-CQDs/SnS_2. The vibrational peaks at 211, 310, and 582 cm^{-1} could be assigned to the first-order E_g mode, A_{1g} mode, and second-order mode E_g of SnS_2, respectively.[37] The peaks at 1600 and 1340 cm^{-1} could be ascribed to the carbon-related Raman-active graphitic (G) and defect (D) bands, respectively.[38] For comparison, Raman spectra of N_{23}-CQDs were also given in the inset of Figure 3.

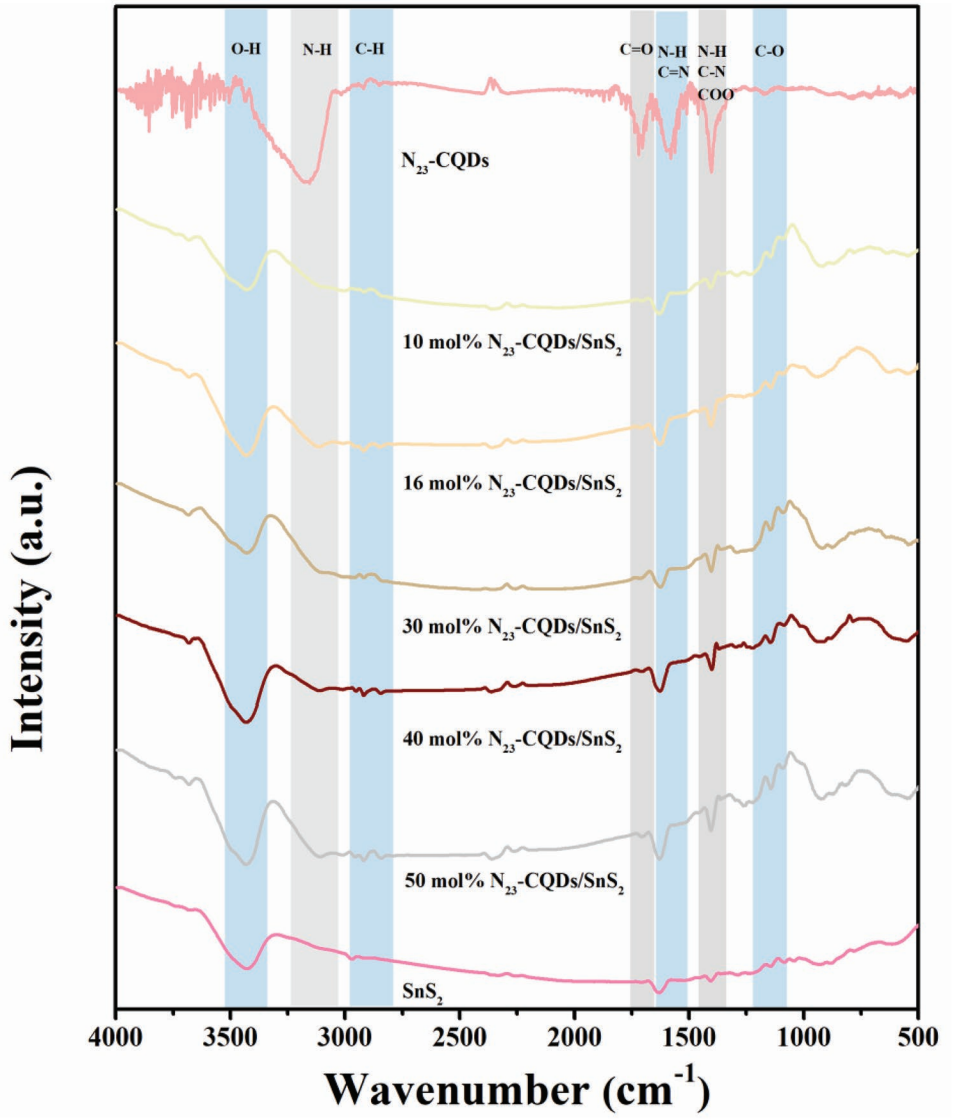

Figure 2. FT-IR spectra of N_{23}-CQDs/SnS_2 loaded with given contents of N_{23}-CQDs. FT-IR spectra of the pristine SnS_2 and N_{23}-CQDs were also given for comparison.

Both N_{23}-CQDs and 40 mol% N_{23}-CQDs/SnS_2 exhibited the same signals as graphitic carbon, which further validated the presence of N_{23}-CQDs in 40 mol% N_{23}-CQDs/SnS_2, as discovered by FT-IR.

To confirm the variations of surface chemical composition and the interaction between N_{23}-CQDs and SnS_2, samples SnS_2, N_{23}-CQDs, and 40 mol% N_{23}-CQDs/SnS_2 were studied by XPS spectra. **Figure 4**a showed a survey spectrum of 40 mol% N_{23}-CQDs/SnS_2, indicating the chemical composition of carbon, nitrogen, and oxygen, in accordance with the results by elemental mapping analysis in Figure S1 (Supporting Information). Considering the trace amount of nitrogen in 40 mol% N_{23}-CQDs/SnS_2, the intensity of N 1s peak is too low to be distinguished from the noise in the survey spectrum. The high-resolution spectra of N 1s in N_{23}-CQDs (Figure 4b) showed three major peaks centered at 399.92, 400.96, and 401.99 eV, which can be assigned to O=N−C, C−N, and C=N groups, respectively, similar to the previous reports on N doped CQDs.[39] However, the peaks related to oxygen-containing O=N−C groups went through a sharp decrease in 40 mol% N_{23}-CQDs/SnS_2. C 1s spectrum in N_{23}-CQDs is composed of four split signals at 284.4, 285.02, 286.46, and 288.52 eV, which could be indexed to C=C/C−C, C−N, C−OH/C−O−C, and C=O/C−O groups, respectively (Figure 4c).[39,40] These also demonstrate the presence of the oxygen-containing functional groups, as documented by FT-IR. For 40 mol% N_{23}-CQDs/SnS_2, the peaks of C−OH/C−O−C and C=O/C−O groups disappeared in C 1s spectra, as observed in N 1s spectra. The similar phenomenon was also observed in O 1s spectra. O 1s spectrum of N_{23}-CQDs in Figure 4d can be deconvoluted and fitted in two peaks at 532.94 and 531.49 eV, which can be assigned to the binding energy of C−OH/C−O−O and C=O, respectively.[40] Compared with N_{23}-CQDs, the intensity of these two peaks in 40 mol% N_{23}-CQDs/SnS_2 was sharply decreased, and O/C ratio

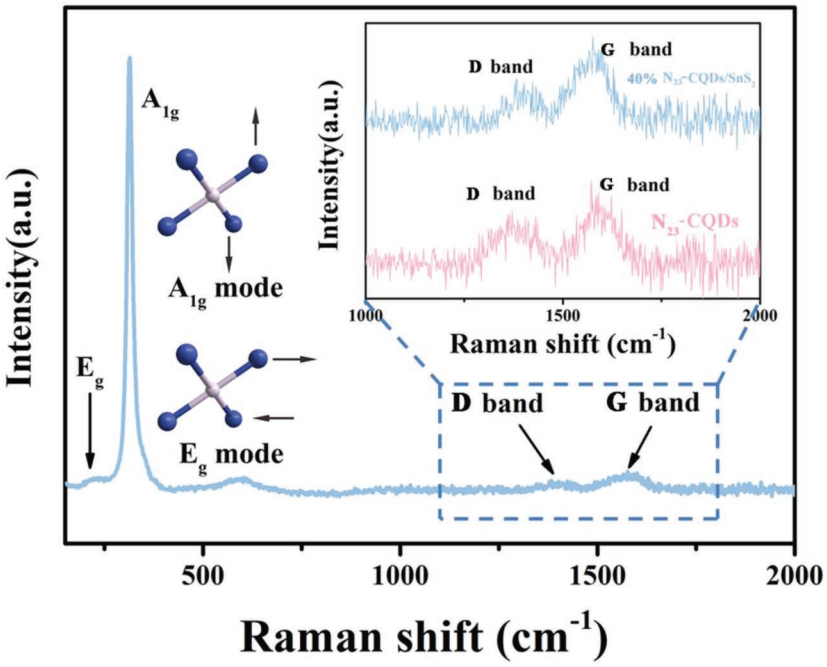

Figure 3. A representative Raman spectrum of 40 mol% N_{23}-CQDs/SnS_2. Inset is the graphitic (G) and defect (D) bands of N_{23}-CQDs and 40 mol% N_{23}-CQDs/SnS_2 in the frequency of 1000–2000 cm^{-1}, respectively.

was dropped from 55.11% in N_{23}-CQDs to 16.16% in 40 mol% N_{23}-CQDs/SnS_2 (Table S1, Supporting Information). As proved by FT-IR, once N_{23}-CQDs were loaded onto SnS_2 nanosheets, the signal of oxygen-containing groups C=O, C—O, C—OH, and C—O—C dramatically decreased, and even disappeared. These could be elucidated by taking into account two primary possibilities: i) N doping in N_{23}-CQDs could promote oxygen-containing functional groups, such as —CO or —COOH groups, adsorbed on the S atoms of SnS_2.[41] Owing to the higher electronegativity of nitrogen (3.0) than carbon (2.5), nitrogen atoms could act as electron acceptor.[39] Therefore, when doped into CQDs, nitrogen is in a state of deficient electrons, which may induce polarization of neighboring oxygen-containing groups and make them more easily attacked by sulfur atom.[42] This was further determined by the changes in bonding energy. As shown in Figure 4b,e, the signals of S 2p as well as N_{23}-CQDs-related signals for C—N and O=C—N deconvoluted in 40 mol% N_{23}-CQDs/SnS_2 exhibited an obvious shift toward lower binding energies when compared with N_{23}-CQDs. For details, both the binding energies of S $2p_{1/2}$ at 161.45 eV and S $2p_{3/2}$ at 162.65 eV in 40 mol% N_{23}-CQDs/SnS_2 are shifted about 0.4 eV toward the lower energy relative to the bonding energy of pristine SnS_2 (Figure 4e). In addition, with regard to N 1s spectrum of 40 mol% N_{23}-CQDs/SnS_2, the bonding energy of C—N group at 401.83 eV was shifted 0.16 eV toward lower energy, and the bonding energy of C=N group at 402 eV was shifted 0.01 eV to the low side relative to those of N_{23}-CQDs (Figure 4b); ii) Oxygen-containing functional groups on the surface of N_{23}-CQDs were mainly phenolic hydroxyl and carboxyl groups, which could provide adsorption sites for metal ions, as reported in literature.[43] As shown in Figure 4f, Sn $3d_{5/2}$ and Sn $3d_{3/2}$ of the pristine SnS_2 are located at 487.1 and 495.5 eV, respectively, with a spin-orbital splitting energy of 8.4 eV. Comparatively, for 40 mol% N_{23}-CQDs/SnS_2, Sn 3d states have an obvious shift toward the low binding energy, in which Sn $3d_{5/2}$ and Sn $3d_{3/2}$ are located at 486.7 and at 495.15 eV, respectively. Hence, a strong interaction is anticipated to occur between N_{23}-CQDs and SnS_2 as 40 mol% N_{23}-CQDs/SnS_2 was formed.

The adsorption of oxygen on N_{23}-CQDs and 40 mol% N_{23}-CQDs/SnS_2 were further investigated by X-ray absorption near-edge structure (XANES). In Figure S2 (Supporting Information), an obvious charge transfer between SnS_2 and N_{23}-CQDs was observed, and the peak position of C=O bond is obviously shifted toward the low-energy direction. The shift is ascribed to the hybridization of the bonding orbitals between SnS_2 and N_{23}-CQDs, which could diminish the energy of C=O (COOH) bond within N_{23}-CQDs, and thus oxygen-containing functional groups on the surface of N_{23}-CQDs have a tremendous decrease. Normalized O K-edge spectra for 40 mol% N_{23}-CQDs/SnS_2 clearly showed a concentration of oxygen-containing functional groups, much lower than those for N_{23}-CQDs. Moreover, the strong interactions were stemmed from the hybrid bonds formed between N_{23}-CQDs and SnS_2 as 40 mol% N_{23}-CQDs/SnS_2 catalyst was synthesized during the in situ hydrothermal process.

2.3. Phase Purity and Crystallinity of N_{23}-CQDs/SnS_2 Loaded with Different Contents of N_{23}-CQDs

Phase purity and crystallinity of N_{23}-CQDs/SnS_2 loaded with different contents of N_{23}-CQDs were examined by X-ray diffraction (XRD). As shown in **Figure 5** and Figure S3 (Supporting Information), XRD patterns of all N_{23}-CQDs/SnS_2 samples exhibited the similar primary diffraction peaks to those of SnS_2. All these diffraction peaks are very sharp, indicating a high crystallinity of the samples. Moreover, all these diffraction peaks could be readily indexed to a hexagonal SnS_2 structure (JCPDS Card No. 23–0677). Whereas, N_{23}-CQDs showed a broad diffraction peak centered at $2\theta = 27°$, which could be attributed to the highly disordered carbon atoms.[25] However, the diffraction peak of N_{23}-CQDs is hard to be detected in the composite because of the weak intensity arising from the low loaded contents.[44] Apparently, the notable difference is detected for the relative intensity of the (001) peak and other diffraction peaks, when compared to unloaded SnS_2 nanosheets. This observation indicates that an interaction does exist between N_{23}-CQDs and SnS_2, which leads to the apparent difference in the crystallite size and preferential orientation of the final products. The composites showed an increasing tendency of the nanosheets that grows along *c*-axis direction. This can be attributed to the following two reasons. First, fresh N-CQDs particles offer abundant functional groups on their surface, serving as nucleation

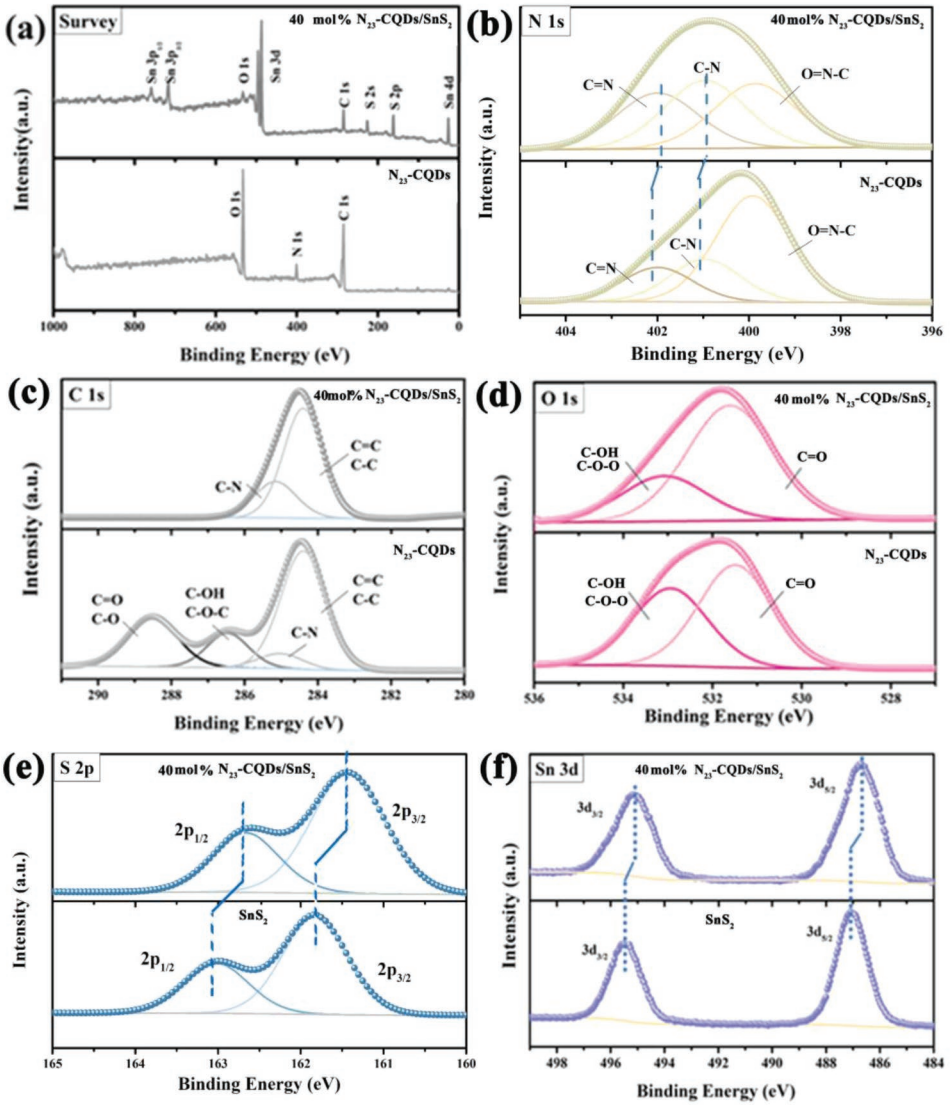

Figure 4. XPS spectra of N_{23}-CQDs, SnS_2, and 40 mol% N_{23}-CQDs/SnS_2: a) survey, b) Sn 3d, c) S 2p, d) C 1s, e) N 1s and f) O 1s.

sites. Second, N_{23}-CQDs tends to induce the stacking of SnS_2 nanosheets.[24] These results are in accordance with TEM data in Figure 1e, evidencing the interaction between SnS_2 and N_{23}-CQDs in 40 mol% N_{23}-CQDs/SnS_2.

2.4. Remarkable Cr(VI) Photoreduction of N-CQDs/SnS_2

Through the above detailed analysis and discussion, N-CQDs/SnS_2 loaded with different contents of N-CQDs was successfully prepared through an in situ loading approach. In the following part, the remarkable photocatalytic activity of N-CQDs/SnS_2 was evaluated in detail using Cr(VI) photoreduction as a modeling reaction. First, the doping amount of N was optimized toward Cr(VI) photoreduction. **Figure 6**a and Figure S4 (Supporting Information) showed the photocatalytic activity of pristine SnS_2, N_{23}-CQDs, N_{13}-CQDs/SnS_2, N_{23}-CQDs/SnS_2, and N_{33}-CQDs/SnS_2. The photocatalytic activity without any catalysts toward Cr(VI) photoreduction is set as a control group. There is no noticeable reduction for the control group, indicating that self-reduction of Cr(VI) could be neglected under visible-light irradiation. There is no photocatalytic activity for N_{23}-CQDs component, as shown in Figure 6a. Photocatalytic activity of the samples loaded with N_{23}-CQDs is much higher than that of pristine SnS_2 (Figure 6). This result can be attributed to the π conjugated systems in N_{23}-CQDs, which could serve as the electron acceptor and promote the transfer of electrons and hinder the recombination of photoinduced electron–hole pairs. N_{23}-CQDs/SnS_2 displays a remarkable photocatalytic activity toward Cr(VI) photoreduction, and 100% of Cr(VI) could be completely reduced after visible light irradiation for 25 min. Photocatalytic activity of N_{23}-CQDs/SnS_2 is the best one, indicating the optimal amount of N doping, i.e., N_{23}. Excessive (N_{13}) or insufficient (N_{33}) N doping is unfavorable to Cr(VI) photoreduction. Moreover, the loading contents of N_{23}-CQDs are expected to have a significant impact on the photocatalytic

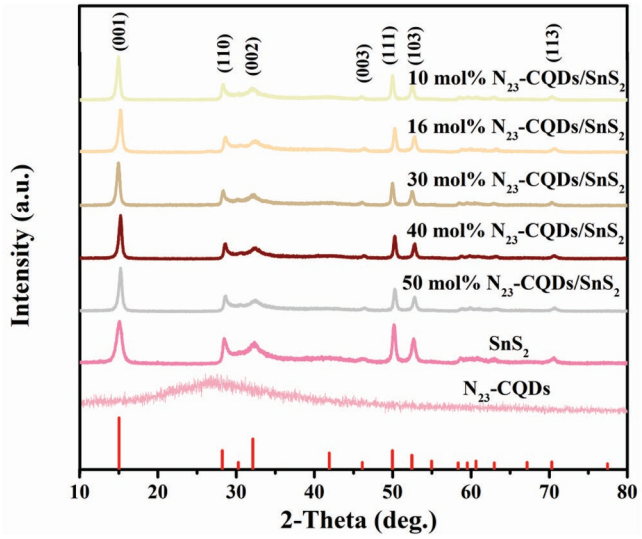

Figure 5. XRD patterns of pristine SnS_2, N_{23}-CQDs, and 40 mol% N_{23}-CQDs/SnS_2 loaded with different loading contents of N_{23}-CQDs. Red vertical bars at the bottom of XRD patterns represent the standard data for hexagonal SnS_2 (JCPDS Card No. 23–0677).

activity of N_{23}-CQDs/SnS_2. As depicted in Figure 6b, the photocatalytic activity increased with N_{23}-CQDs, and the sample loaded with 40 mol% N_{23}-CQDs has the best photocatalytic activity. This can be rationalized that at low loading contents, N_{23}-CQDs could significantly separate the photoinduced charges in the conduction band of SnS_2 and thus efficiently improve the photocatalytic activity. However, although N_{23}-CQDs favored the charge separation, excessive N_{23}-CQDs accumulated on the surface of SnS_2 would shield SnS_2 from absorbing visible light.[45] This hypothesis is supported by the following experiment result. For the present Cr(VI) photoreduction system, the photocatalytic reaction is triggered by capturing the visible light. The lower light harvesting rate SnS_2 has, the lower photocatalytic activity would be. This is why 50 mol% N_{23}-CQDs/SnS_2 possesses a lower activity in the visible light, when comparing to 40 mol% N_{23}-CQDs/SnS_2.

For comparison, the curves of the photocatalytic activity for all samples are fitted by a pseudo-first-order reaction

$$\ln(C/C_0) = kt \quad (1)$$

where k is the constant of the first-order kinetic rate; C_0 is the initial concentration after dark reaction; C is the instant

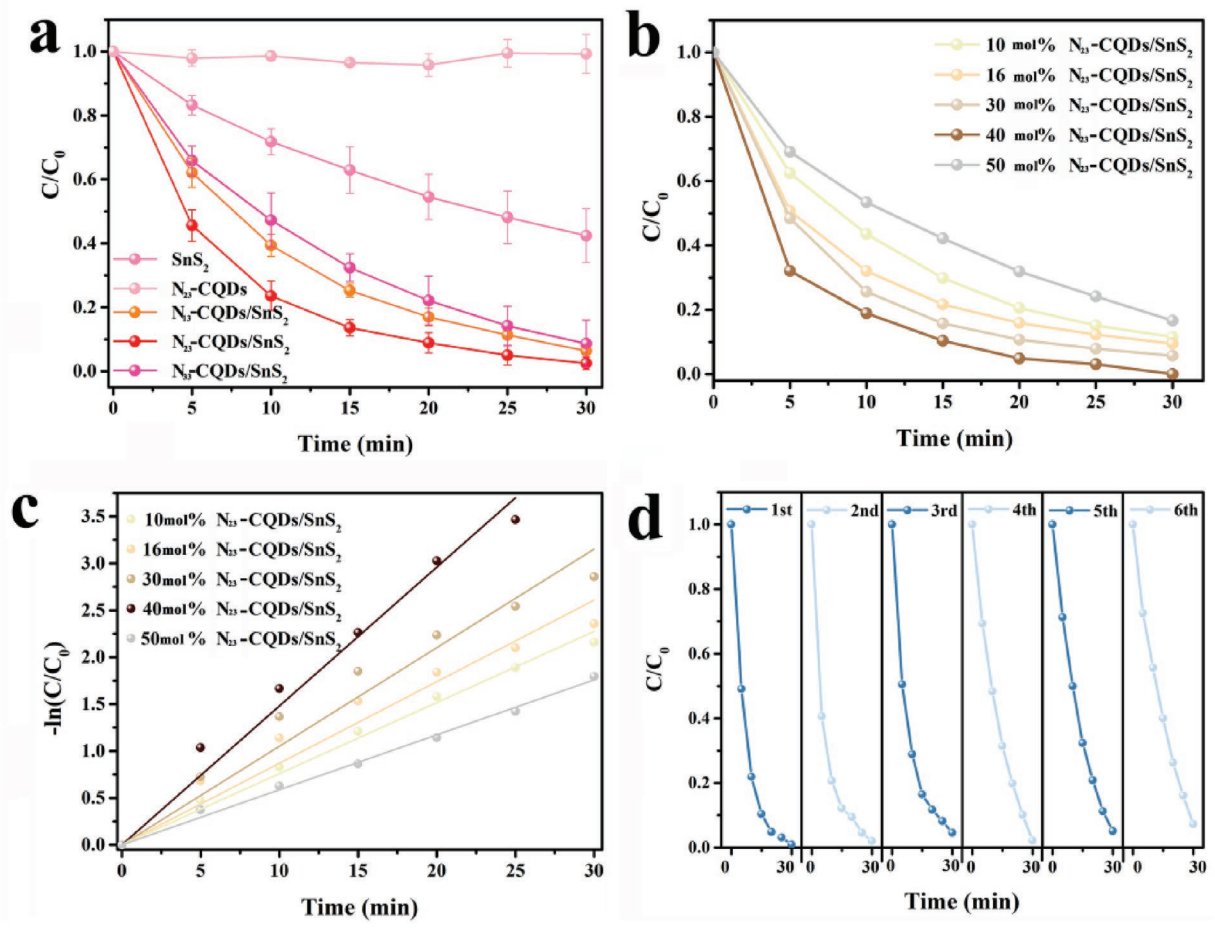

Figure 6. a,b) Photocatalytic activity and c) kinetic curves fitting of Cr(VI) photoreduction at the fixed time intervals for pristine SnS_2, N_{23}-CQDs, and N_{23}-CQDs/SnS_2 loaded with different N_{23}-CQDs contents under visible light irradiation ($\lambda > 400$ nm). d) Recycling performance of 40 mol% N_{23}-CQDs/SnS_2 for Cr(VI) photoreduction.

concentration with the irradiation time *t*. As shown in Figure 6c and Figure S5 (Supporting Information), the fitting curves are nearly linear. The constants (*k*) of the pseudo-first-order kinetic rate are calculated and summarized in Table S1 (Supporting Information). As listed in Table S1 (Supporting Information), all N_{23}-CQDs/SnS_2 catalysts have remarkable photocatalytic activity toward Cr(VI) photoreduction, among which 40 mol% N_{23}-CQDs/SnS_2 catalyst has the biggest *k* value, which is 148 times higher than bare N_{23}-CQDs and 5 times higher than the pristine SnS_2.

Considering the photocorrosion of metal sulfides,[46] it is critically important to investigate the photostability of all N_{23}-CQDs/SnS_2 catalysts. The photostability of the as-prepared 40 mol% N_{23}-CQDs/SnS_2 catalyst is taken as an example. Figure 6d showed the recycling performance of 40 mol% N_{23}-CQDs/SnS_2 catalyst after completing 6 cycles of Cr(VI) photoreduction. The photocatalytic activity was just decreased less than 10% after 6 cycles compared with the first one, indicating a much high photostability. Moreover, 40 mol% N_{23}-CQDs/SnS_2 catalyst showed slight changes in the crystal structures and morphology after 6 cycles, as shown in Figures S6 and S7 (Supporting Information), which suggested an improved life in service.

2.5. Mechanisms for the Remarkable Cr(VI) Photoreduction of N-CQDs/SnS_2

To uncover the mechanism for the remarkable Cr(VI) photoreduction of 40% N_{23}-CQDs/SnS_2, the visible light absorption and optical bandgap were characterized by UV–Vis diffuse reflectance spectra. As the main component of 40 mol% N_{23}-CQDs/SnS_2, SnS_2 shows a light absorption that covers the entire visible-light region due to the intrinsic band-to-band transition and strong tail absorption (Urbach tail) (**Figure 7**a). With regard to N_{23}-CQDs, an intense absorption is at 200–1000 nm, which could be assigned to n–p* transition of C=O bond and p–p* transition of aromatic C=C bonds.[31,44] Even though the light absorption of N_{23}-CQDs almost covered the full spectrum, the bare N_{23}-CQDs has a poor Cr(VI) photoreduction performance. This can be ascribed to the abundant oxygen-containing functional groups on the surfaces of N_{23}-CQDs, which could serve as the quenching centers of photogenerated electrons, limiting the photocatalytic activity. For N_{23}-CQDs loading onto SnS_2 nanosheets, oxygen-containing groups dramatically decreased and even disappeared in N_{23}-CQDs/SnS_2 catalyst, as evidenced by IR, XPS, and XANES (Figure S2, Supporting Information). In this case, the fractional surface of N_{23}-CQDs without oxygen-containing functional groups could form a strong interaction interface with SnS_2. The introduction of N_{23}-CQDs also brought about a red shift in adsorption spectra, as observed in other metal-loaded systems.[47] The content of N_{23}-CQDs in 40 mol% N_{23}-CQDs/SnS_2 was much lower than that of SnS_2, and thus N_{23}-CQDs served as a photosensitizer. Meanwhile, N_{23}-CQDs loading could create a midgap state (sub-bandgap) that allows catalysts to absorb lower energy photons than the actual optical bandgap[48] and provides the localized energy levels for the photogenerated charge carriers. This can effectively suppress the recombination of the photogenerated charge carriers, resulting in a remarkable photocatalytic activity.[49]

The optical bandgap was further studied, as shown in Tauc plots of Figure 7b.[50] Based on the literature reports,[51–53] SnS_2 is a direct bandgap semiconductor. Hence, the transition energy (E_t) of SnS_2 is calculated to be 2.18 eV by the Kubelk–Munk method which is of a direct-type semiconductor through the theory of optical absorption (Equation (2)) (Figure 7b)[54]

$$\alpha h\nu = B(h\nu - E)^{1/2} \tag{2}$$

Compared to the absorption bandedge of pristine SnS_2 (Figure 7a), 40 mol% N_{23}-CQDs/SnS_2 catalyst showed a broader absorption bandedge. Hence, N_{23}-CQDs loading could effectively tune the electronic structure, improve the visible light absorption, and further enhance the photocatalytic activity. To further reveal the detailed band structure of 40 mol% N_{23}-CQDs/SnS_2 catalyst for better understanding the mechanism of Cr(VI) photoreduction, it is essential to determine the position of the bandgap. The electrochemical Mott–Schottky plot in the darkness was first performed to acquire the flatband position of SnS_2, as shown in Figure 7c. The positive slope of the straight line indicated that SnS_2 is a n-type semiconductor. In this case, the flat-band potential can be estimated to equal the corresponding its conduction band minimum, with minor deviation of less than 0.1 eV.[55] The flat-band potential of SnS_2 is –0.8 V versus Ag/AgCl electrode, corresponding to –0.19 V versus reversible hydrogen electrode. Combined with the obtained bandgap energy in Figure 7b, the position of the valence band of SnS_2 was determined. As depicted in Figure 7d, the valence band maximum for SnS_2 was 1.99 eV, whereas the conduction band minimum was –0.19 eV.

Based on the experimental data analyses about bandgap energy, bandgap position, and energy band theories of semiconductors, the mechanism of photoreduction and photodegradation for N_{23}-CQDs/SnS_2 catalysts was proposed. N_{23}-CQDs/SnS_2 catalysts could be excited by visible light to generate electron–hole charge pairs, in which electrons are transferred from the valence band to the conduction band, leaving the holes on the valence band. Since the redox potential of $Cr_2O_7^{2-}/Cr^{3+}$ (1.232 V) is lower than the CB level of SnS_2, the photoexcited electrons could be easily delivered to Cr(VI) to form Cr(III), while H_2O molecules capture the holes on the valence band to produce molecular oxygen. Then, Cr(VI) photoreduction is ended.

However, these electron–hole charge pairs tend to recombine quickly, and only part of charges could be involved in photocatalytic process. To accelerate Cr(VI) photoreduction through effectively utilizing the holes, another common organic pollutant in the tannery wastewater, "4-NP," as a hole sacrificing agent. It is noted that light absorptions of 4-NP and Cr(VI) are mainly from ultraviolet light and a small amount of visible light, which are almost not competing with the photocatalysts for the absorption of visible light. The photocatalytic activities of N_{23}-CQDs/SnS_2 catalysts with different amounts of doping N and loaded with different contents of N_{23}-CQDs, under the conditions with and without 4-NP in 5 min, respectively, are shown in Figure 7e,f. Figure S8 (Supporting Information) showed the corresponding UV–Vis spectra for the samples loaded with different contents of N_{23}-CQDs. In combination with 4-NP, both photogenerated electrons and holes could be sufficiently utilized, which could

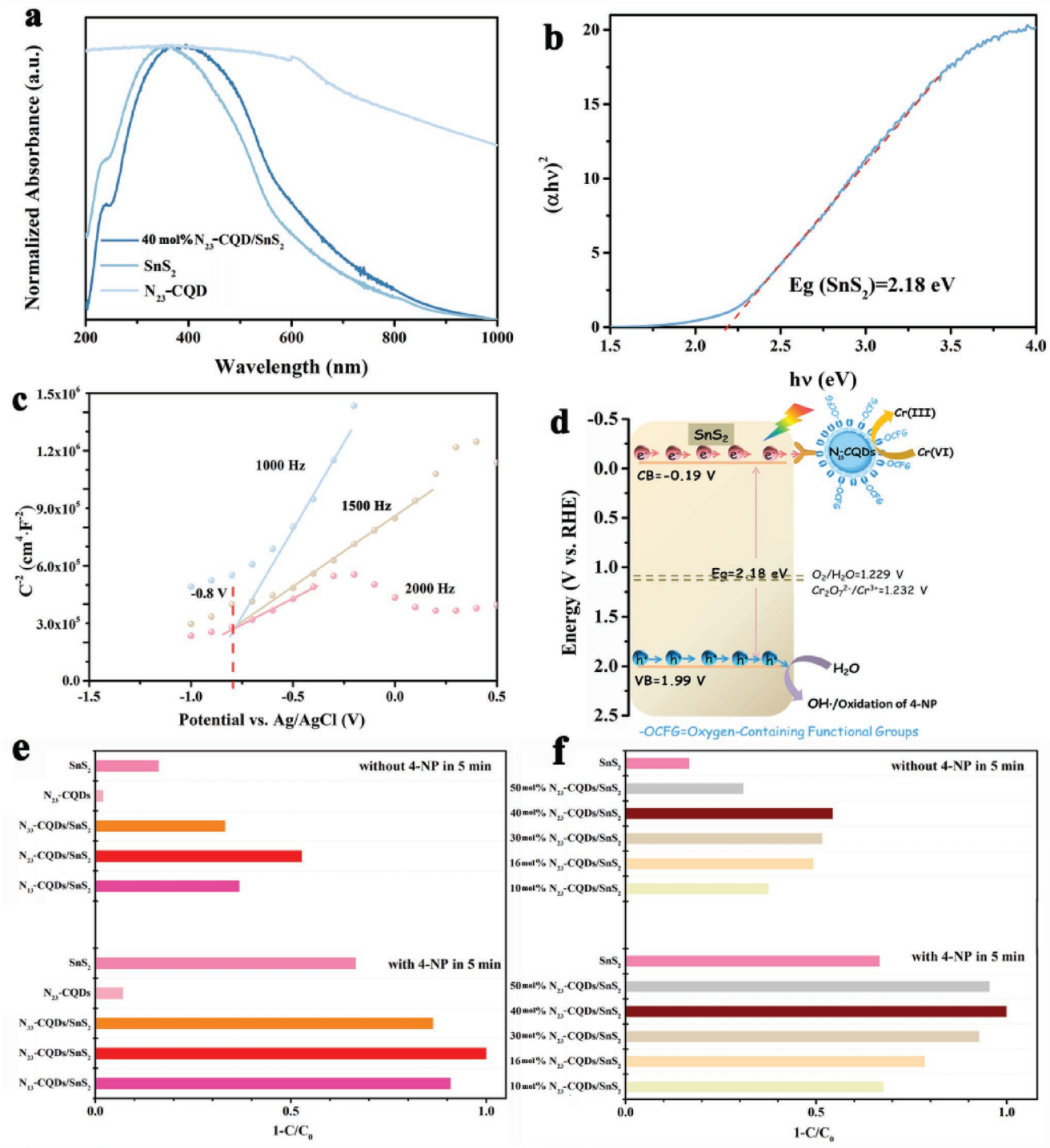

Figure 7. a) Normalized UV–Vis diffuse reflectance spectra of the pristine SnS_2, N_{23}-CQDs, and 40 mol% N_{23}-CQDs/SnS_2. b) Tauc plots of the pristine SnS_2 catalyst. c) Mott–Schottky curves for SnS_2 nanosheets collected at various frequencies (pH = 7). d) Schematic mechanism for Cr(VI) photoreduction at the interface between SnS_2 and N_{23}-CQDs. e,f) Performance comparison of Cr(VI) photoreduction for N_{23}-CQDs/SnS_2 loaded with different contents of N_{23}-CQDs without 4-NP and in the presence of 4-NP for 5 min under visible-light irradiation.

promote the efficiency of the charge separation and transfer, and further significantly improve the photocatalytic activity. Remarkably, the photocatalytic activity of N_{23}-CQDs/SnS_2 catalysts loaded with 40 mol% N_{23}-CQDs is the best, which completed 100% Cr(VI) photoreduction in just 5 min (Figure 7e,f). We attribute this fast photoreduction to the fact that 4-NP captures photogenerated holes and improves charge separation efficiency. Moreover, N_{23}-CQDs have delocalized conjugated structure that makes the electrons easily transfer and separate from holes. Therefore, N_{23}-CQDs loaded on SnS_2 nanosheets

could effectively tune the electronic structures and significantly enhance photocatalytic activity toward Cr(VI) photoreduction. To further confirm this point, the behaviors of separation and transfer of photogenerated charge carriers were further investigated by the SPV and EIS.

2.6. Photogenerated Charge Transfer of the Samples

SPV response for a nanosized catalyst is mainly from the separation of photogenerated charge carriers via a diffusion process,[56] thus SPV can provide important information about the separation and recombination of photogenerated charge carriers. The higher signal of SPV response represents the higher separation rate of photogenerated charges carriers. In this work, SPV technique was utilized to evaluate the role of N_{23}-CQDs loading in the separation and transfer of photoexcited charge carriers. As shown in **Figure 8**a, the onset energy of 40 mol% N_{23}-CQDs/SnS_2 catalyst is lower than both N_{23}-CQDs and pristine SnS_2, which demonstrated that the introduction of N_{23}-CQDs reduced the photon energy required for the band-to-band transition of electrons, consistent with the results by UV–Vis diffuse reflectance spectra. Moreover, 40 mol% N_{23}-CQDs/SnS_2 catalyst has a stronger SPV response when compared with N_{23}-CQDs and SnS_2 in the high region of photon energy (photon energy > 2 eV). The maximum SPV amplitude response of 40 mol% N_{23}-CQDs/SnS_2 catalyst is 159 μV, which is dramatically higher than that of SnS_2 at 17 μV and N_{23}-CQDs at 124 μV. These observations proved that N_{23}-CQDs loading significantly enhanced the separation of photoexcited charge carriers. Further, all characteristic peaks of N_{23}-CQDs are displayed in 40 mol% N_{23}-CQDs/SnS_2, confirming the presence of N_{23}-CQDs in the composite again, in accordance with the abovementioned analyses by FT-IR, XPS, and Raman.

EIS measurement was carried out to study the interfacial charge transfer rate of the as-prepared samples, as shown in Figure 8b. 40 mol% N_{23}-CQDs/SnS_2 catalyst has the least arc radius on the EIS Nynquist plot when compared with those of the pristine SnS_2 and bare N_{23}-CQDs. The smallest arc radius in EIS Nynquist plot demonstrated the minimum resistance of interfacial charge transfer, giving the highest efficiency of the charge separation. Hence, 40 mol% N_{23}-CQDs/SnS_2 catalyst loaded with N_{23}-CQDs has a high separation rate of photoinduced electron–hole charge pairs and a fast interfacial charge transfer rate to accelerate Cr(VI) photoreduction reaction.

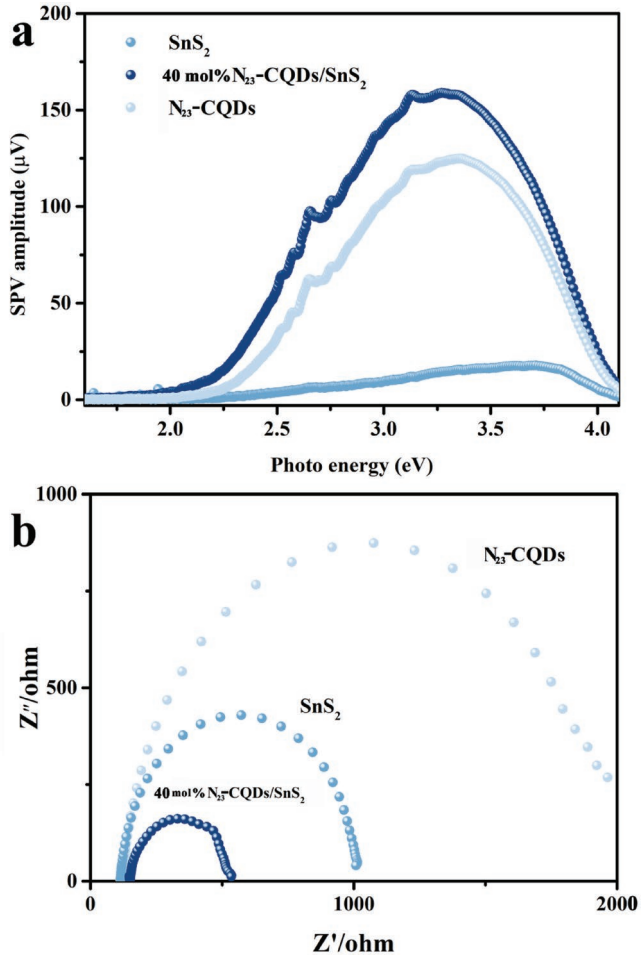

Figure 8. a) SPV spectra and b) EIS Nyquist plots of SnS_2, N_{23}-CQDs, and 40 mol% N_{23}-CQDs/SnS_2.

3. Conclusion

A series of in situ N-CQD loaded SnS_2 were prepared and well characterized. Cr(VI) photoreduction was examined, and the optimal N doping amounts in N-CQDs/SnS_2 and N_{23}-CQDs loading contents in N_{23}-CQDs/SnS_2 were determined. 40 mol% N_{23}-CQDs/SnS_2 catalyst showed an ultrahigh kinetic rate constant of 0.148 min^{-1} with a promising potential for leather wastewater treatment. N_{23}-CQDs loading could improve the photocatalytic performance of the corresponding composite catalysts, since N_{23}-CQDs provided a delocalized conjugated structure that facilitates the separation and transfer of photogenerated charge carriers. Moreover, 4-NP serves as a hole-acceptor that further improves photocatalytic performance, since it captures the photogenerated holes and hinders the combination of electron–hole pairs. The method reported in this work could be applicable in seeking for more advanced catalyst with non-noble metals, but also could provide an avenue for advanced green chemistry, environmental harness, and high-performance optoelectronic devices.

4. Experimental Section

Synthesis of SnS_2 Nanosheets: All chemicals were of analytical grade and used as received without further treatment. SnS_2 nanosheets were prepared according to a process reported with some modifications.[57] In a typical experiment, $SnCl_4$ and thioacetamide (TAA) at a molar ratio of $SnCl_4$:TAA = 1:3 were mixed and dissolved in 70 mL distilled water under vigorous stirring to form a homogeneous solution at room temperature. Subsequently, the obtained solution was transferred to a Teflon-lined stainless-steel autoclave, which was subjected to reaction at 463 K for 6 h. Finally, the resultant was collected by centrifugation, washed with water and ethanol several times, and dried at 60 °C for 12 h for further characterization and synthesis of N-CQDs/SnS_2 catalysts. The collected sample is denoted as SnS_2 nanosheets.

Synthesis of N-CQDs Quantum Dots: N-CQDs were synthesized based on a previous method with some modifications.[58] In a typical experiment, citric acid (CA) and urea (UA) at a molar ratio of 2:3 (1.2 mmol:1.8 mmol) were dissolved in 25 mL distilled water, under vigorous stirring, to form a transparent solution. Then, the solution was transferred to a 100 mL Teflon-lined stainless-steel autoclave with a filling (capacity of 25%) and heated at 160 °C for 4 h. The autoclave was allowed to cool naturally to room temperature. The resulting solution was precipitated through adding excessive ethanol. Finally, the precipitate was collected by centrifugation, washed with water and ethanol several times, and dried in a freeze dryer for 48 h. The collected sample is denoted as N_{23}-CQDs.

Synthesis of N-CQDs/SnS_2 Catalysts with Different N Doping Amounts: An in situ route was initiated to synthesize N-CQDs/SnS_2 catalyst. N-CQDs/SnS_2 with different N doping amounts was fabricated by adjusting the mole ratio of CA to UA. Specifically, 3 mmol of the as-prepared SnS_2 nanosheets was added to the mixture of CA and UA at a certain molar ratio. After vigorously stirring for 30 min, the obtained suspension was transferred into a Teflon-lined stainless-steel autoclave and heated at 433 K for 4 h. The autoclave was allowed to cool naturally to room temperature. Finally, the resultant was collected by centrifugation, washed with water and ethanol several times, and dried at 353 K overnight for further characterization. The obtained samples with mole ratio of CA:UA at 1:3 (1.2 mmol:3.6 mmol), 2:3 (1.2 mmol:1.8 mmol), and 3:3 (1.2 mmol:1.2 mmol) were named as N_{13}-CQDs/SnS_2, N_{23}-CQDs/SnS_2, N_{33}-CQDs/SnS_2, respectively. The actual N doping amount of the as-prepared samples was measured by elemental analysis and the data were listed in Table S1 (Supporting Information).

Synthesis of N_{23}-CQDs/SnS_2 Catalysts with Different N_{23}-CQDs Loading Contents: To prepare N_{23}-CQDs/SnS_2 with different N_{23}-CQDs loading contents, SnS_2 was fixed at 3 mmol with altered total amount of CA and UA, while the molar ratio of CA and UA was kept at 2:3. The preparation procedure is similar to that for N_{23}-CQDs/SnS_2 with different N doping amounts. For simplicity, the samples were named using the initial molar ratio of UA to SnS_2 as the loading content of N_{23}-CQDs. The obtained samples were denoted as 10 mol% N_{23}-CQDs/SnS_2 (CA:UA = 0.3 mmol:0.45 mmol), 16 mol% N_{23}-CQDs/SnS_2 (CA:UA = 0.5 mmol:0.75 mmol), 30 mol% N_{23}-CQDs/SnS_2 (CA:UA = 0.9 mmol:1.35 mmol), 40 mol% N_{23}-CQDs/SnS_2 (CA:UA = 1.2 mmol:1.8 mmol), 50 mol% N_{23}-CQDs/SnS_2 (CA:UA = 1.5 mmol:2.25 mmol), respectively. The actual N_{23}-CQDs loading contents of the as-prepared samples were measured by CHNS elemental analysis, and the data of C% were listed in Table S1 (Supporting Information).

Photocatalytic Activity: i) Cr(VI) photoreduction: Photocatalytic activity was evaluated by Cr(VI) reduction in a customized photochemical reactor with cooling attachments using a 300 W Xe lamp coupled with 400 nm cutoff filters as a light source (PLS-SXE 300; Beijing Perfectlight). All experiments were carried out at 20 ± 2 °C using a water bath cooling system. In a typical reaction, 30 mg of the as-prepared photocatalyst was dispersed in 30 mL of Cr(VI) solution (50 mg L^{-1} $K_2Cr_2O_7$) under ultrasonic vibration. Subsequently, the suspension was subjected to a dark treatment for 2 h to reach adsorption–desorption equilibrium. During the visible-light illumination, 0.3 mL of suspension was taken out each time from the reactor at a time interval of 5 min. The supernatant was collected by filtration using a cellulose acetate membrane filter with pore size of 0.22 nm. Then, the supernatant was analyzed by the UV–Vis spectroscopy using the diphenylcarbazide method.[59] The Cr(VI) reduction percentage = $C/C_0 = A_t/A_0$, where A_0 and C_0 are the absorbance and concentration of the Cr(VI) solution after dark treatment, respectively; A_t and C are the absorbance and concentration of the remnant Cr(VI) after a given irradiation period, respectively. ii) To further improve the photocatalytic activity of N-CQDs/SnS_2 catalysts with different N doping amounts and N_{23}-CQDs/SnS_2 catalysts with different N_{23}-CQDs loading contents, 4-NP was utilized as a hole acceptor to accelerate the Cr(VI) photoreduction. Specifically, 30 mg of photocatalyst was dispersed in the mixture of 30 mL $K_2Cr_2O_7$ (50 mg L^{-1}) and 10 mL 4-NP (10 mg L^{-1}) aqueous solution with vigorous stirring. Prior to the visible-light illumination, the system was kept in dark for 2 h to reach an adsorption–desorption equilibrium. During the visible-light illumination ($\lambda > 400$ nm), 0.3 mL of the suspension taken out each time from the reactor was at a time interval of 3 min. The following analytical protocol is same as the abovementioned (i).

Photocatalytic Stability: 40 mol% of the N_{23}-CQDs/SnS_2 catalysts were recycled six times under the same condition. The aged catalyst after 30 min cycles was separated by filtration and washed to remove the remaining Cr(VI) on the surface of the catalysts. The collected catalysts were dried and weighed for the next cycle, i.e., the catalysts used in each cycle is the remained catalyst from the last one.

Electrochemical Characterization: The electrochemical properties were executed on an electrochemical workstation (CHI 760E) using a three-electrode system in a 0.2 M Na_2SO_4 electrolyte (pH = 7). Pt wire is a counter electrode and silver–silver chloride (Ag/AgCl, saturated KCl) is a reference electrode, and the as-prepared photocatalysts serve as a working electrode with a surface area of 0.173 cm^2. All the working electrodes were prepared using a spin-coating technique with same conditions. Specifically, 0.05 g of photocatalyst was mixed with 450 µL distill water, 500 µL ethanol, and 5 µL Nafion to form a slurry under ultrasonic vibration. Then, the slurry was then spin-coated on a 1.5 cm × 2 cm fluorine-doped tin oxide (FTO) glass electrode. The obtained glass electrode was heated at 673 K for 1 h under a N_2 flow. Mott–Schottky plots were collected at a frequency of 1000, 2000, and 3000 Hz, respectively. The EIS measurements were performed at –1.4 V versus Ag/AgCl in a frequency ranging from 0.1 Hz to 10 kHz with an alternating (AC) sinusoidal perturbation of 10 mV. For details about equipment, please check the Supporting Information.

Supporting Information

Supporting Information is available from the Wiley Online Library or from the author.

Acknowledgements

This work was financially supported by National Natural Science Foundation of China (NSFC) (Grant Nos. 21671077, 21771075, 21571176, and 21871106). The authors acknowledge the National Synchrotron Radiation Laboratory (NSRL) beamline BL12B-a for providing beam time.

Conflict of Interest

The authors declare no conflict of interest.

Keywords

carbon quantum dots, green chemistry, in situ synthesis, photogenerated charge carrier, tannery wastewater processing

Received: October 29, 2018
Revised: December 29, 2018
Published online: February 8, 2019

[1] G. Lofrano, S. Meric, G. E. Zengin, D. Orhon, *Sci. Total Environ.* **2013**, *461–462*, 265.
[2] A. A. Nafiey, A. Addad, B. Sieber, G. Chastanet, A. Barras, S. Szunerits, R. Boukherroub, *Chem. Eng. J.* **2017**, *322*, 375.

[3] P. Wang, X. Yi, Y. Lu, H. Yu, J. Yu, *J. Colloid Interface Sci.* **2018**, *532*, 272.
[4] M. Tasbihi, F. Fresno, U. Simon, I. J. V. García, V. P. Dieste, C. Escudero, V. A. P. O'Shea, *Appl. Catal., B* **2018**, *239*, 68.
[5] A. Shi, H. Li, , S. Yin, Z. Hou, J. Rong, J. Zhang, Y. Wang, *Appl. Catal., B* **2018**, *235*, 197.
[6] M. Ji, X. Su, Y. Zhao, W. Qi, Y. Wang, G. Chen, Z. Zhang, *Appl. Surf. Sci.* **2015**, *344*, 128.
[7] S. J. Santosa, D. Siswanta, S. Sudiono, R. Utarianingrum, *Appl. Surf. Sci.* **2008**, *254*, 7846.
[8] D. Li, S. Yu, H. Jiang, *Adv. Mater.* **2018**, *30*, 1707377.
[9] J. Xiao, H. Jiang, *Small* **2017**, *13*, 1700632.
[10] T. Yan, J. Tian, W. Guan, Z. Qiao, W. Li, J. You, B. Huang, *Appl. Catal., B* **2017**, *202*, 84.
[11] S. Azimi, A. N. Ejhieh, *J. Mol. Catal. A: Chem.* **2015**, *408*, 152.
[12] C. Xie, X. Lu, F. Deng, X. Luo, J. Gao, D. D. Dionysiou, *Chem. Eng. J.* **2018**, *338*, 591.
[13] S. Sehati, M. H. Entezari, *Sep. Purif. Technol.* **2017**, *174*, 482.
[14] Z. Cheng, F. Wang, T. A. Shifa, C. Jiang, Q. Liu, J. He, *Small* **2017**, *13*, 1702163.
[15] L. Jing, Y. Xu, Z. Chen, M. He, M. Xie, J. Liu, H. Xu, S. Huang, H. Li, *ACS Sustainable Chem. Eng.* **2018**, *6*, 5132.
[16] S. Guo, X. Li, J. Zhu, T. Tong, B. Wei, *Small* **2016**, *12*, 5692.
[17] M. A. Holmes, T. K. Townsend, F. E. Osterloh, *Chem. Commun.* **2012**, *48*, 371.
[18] Y. Huang, Y. Liang, Y. Rao, D. Zhu, J. Cao, Z. Shen, W. Ho, S. C. Lee, *Environ. Sci. Technol.* **2017**, *51*, 2924.
[19] H. Zhang, H. Huang, H. Ming, H. Li, L. Zhang, Y. Liu, Z. Kang, *J. Mater. Chem.* **2012**, *22*, 10501.
[20] M. Rehberg, K. Nekolla, S. Sellner, M. Praetner, K. Mildner, D. Zeuschner, F. Krombach, *Small* **2016**, *12*, 1882.
[21] M. Balogun, Y. Luo, F. Lyu, F. Wang, H. Yang, H. Li, C. Liang, M. Huang, Y. Huang, Y. Tong, *ACS Appl. Mater. Interfaces* **2016**, *8*, 9733.
[22] K. Jiang, S. Sun, L. Zhang, Y. Lu, A. Wu, C. Cai, H. Lin, *Angew. Chem., Int. Ed.* **2015**, *54*, 5360.
[23] H. Yu, R. Shi, Y. Zhao, G. I. N. Waterhouse, L. Wu, C. Tung, T. Zhang, *Adv. Mater.* **2016**, *28*, 9454.
[24] J. Di, J. Xia, M. Ji, L. Xu, S. Yin, Q. Zhang, Z. Chen, H. Li, *Carbon* **2016**, *98*, 613.
[25] J. Xia, J. Di, H. Li, H. Xu, H. Li, S. Guo, *Appl. Catal., B* **2016**, *181*, 260.
[26] L. Li, X. Zhu, ACS Appl. *ACS Appl. Nano Mater.* **2018**, *1*, 5337.
[27] L. Li, X. Zhu, *ACS Appl. Nano Mater.* **2018**, *1*, 5337.
[28] J. Di, J. Xia, M. Ji, B. Wang, S. Yin, H. Xu, Z. Chen, H. Li, *Langmuir* **2016**, *32*, 2075.
[29] G. Li, R. Su, J. Rao, J. Wu, P. Rudolf, G. R. Blake, R. A. Groot, F. Besenbacher, T. T. M. Palstra, *J. Mater. Chem. A* **2016**, *4*, 209.
[30] J. Tan, R. Zou, J. Zhang, W. Li, L. Zhang, D. Yue, *Nanoscale* **2016**, *8*, 4742.
[31] Q. Liang, W. Ma, Y. Shi, Z. Li, X. Yang, *Carbon* **2013**, *60*, 421.
[32] P. Hsu, H. Chang, *Chem. Commun.* **2012**, *48*, 3984.
[33] S. Zhu, J. Zhang, S. Tang, C. Qiao, L. Wang, H. Wang, X. Liu, B. Li, Y. Li, W. Yu, X. Wang, H. Sun, B. Yang, *Adv. Funct. Mater.* **2012**, *22*, 4732.
[34] D. Sun, R. Ban, P. Zhang, G. Wu, J. Zhang, J. Zhu, *Carbon* **2013**, *64*, 424.
[35] X. Miao, D. Qu, D. Yang, B. Nie, Y. Zhao, H. Fan, Z. Sun, *Adv. Mater.* **2018**, *30*, 1704740.
[36] C. Zhu, J. Zhai, S. Dong, *Chem. Commun.* **2012**, *48*, 9367.
[37] Y. Ren, J. Wang, X. Huang, J. Ding, *Mater. Lett.* **2017**, *186*, 57.
[38] S. Muthulingam, K. B. Bae, R. Khan, I-H. Lee, P. Uthirakumar, *RSC Adv.* **2015**, *5*, 46247.
[39] Y. Yang, W. Kong, H. Li, J. Liu, M. Yang, H. Huang, Y. Liu, Z. Wang, Z. Wang, T. Sham, J. Zhong, C. Wang, Z. Liu, S-T. Lee, Z. Kang, *ACS Appl. Mater. Interfaces* **2015**, *7*, 27324.
[40] A. Alam, B. Park, Z. Ghouri, M. Park, H. Kim, *Green Chem.* **2015**, *17*, 3791.
[41] J. Song, T. Xu, M. L. Gordin, P. Zhu, D. Lv, Y. Jiang, Y. Chen, Y. Duan, D. Wang, *Adv. Funct. Mater.* **2014**, *24*, 1243.
[42] W. H. Shin, H. M. Jeong, B. G. Kim, J. K. Kang, J. W. Choi, *Nano Lett.* **2012**, *12*, 2283.
[43] Y. Bian, Z. Bian, J. Zhang, A. Ding, S. Liu, H. Wang, *Appl. Surf. Sci.* **2015**, *329*, 269.
[44] J. Di, J. Xia, Y. Ge, H. Li, H. Ji, H. Xu, Q. Zhang, H. Li, M. Li, *Appl. Catal., B* **2015**, *168–169*, 51.
[45] Y. Han, H. Huang, H. Zhang, Y. Liu, X. Han, R. Liu, H. Li, Z. Kang, *ACS Catal.* **2014**, *4*, 781.
[46] C. Wang, L. Wang, J. Jin, J. Liu, Y. Li, M. Wu, L. Chen, B. Wang, X. Yang, B. Su, *Appl. Catal., B* **2016**, *188*, 351.
[47] Y. Zhou, P. Lv, W. Zhang, X. Meng, H. He, X. Zeng, X. Shen, *Appl. Surf. Sci.* **2018**, *457*, 925.
[48] J. Ran, T. Ma, G. Gao, X. Du, S. Qiao, *Energy Environ. Sci.* **2015**, *8*, 3708.
[49] C. H. Choi, L. Lin, S. Gim, S. Lee, H. Kim, X. Wang, W. Choi, *ACS Catal.* **2018**, *8*, 4241.
[50] P. Niu, Y. Yang, J. Yu, G. Liu, H. Cheng, *Chem. Commun.* **2014**, *50*, 10837.
[51] S. Wang, G. Li, Z. Leng, Y. Wang, S. Fang, J. Wang, Y. Wei, L. Li, *Appl. Surf. Sci.* **2019**, *471*, 813.
[52] G. Zhang, D. Chen, N. Li, Q. Xu, H. Li, J. He, J. Lu, *J. Colloid Interface Sci.* **2018**, *514*, 306.
[53] Y. Zhang, Z. Du, K. Li, M. Zhang, D. D. Dionysiou, *ACS Appl. Mater. Interfaces* **2011**, *3*, 1528.
[54] N. Zhang, L. Li, G. Li, *Res. Chem. Intermed.* **2017**, *43*, 5011.
[55] Q. Guo, H. Li, Q. Zhang, Y. Zhang, *Appl. Catal., B* **2018**, *229*, 192.
[56] N. Zhang, G. Li, T. Xie, L. Li, *J. Colloid Interface Sci.* **2018**, *525*, 196.
[57] Z. Zhang, J. Huang, M. Zhang, Q. Yuan, B. Dong, *Appl. Catal., B* **2015**, *163*, 298.
[58] W. Yang, L. Zhang, Y. Hu, Y. Zhong, H. Wu, X. W. (David) Lou, *Angew. Chem., Int. Ed.* **2012**, *51*, 11501.
[59] D. Qu, M. Zheng, P. Du, Y. Zhou, L. Zhang, D. Li, H. Tan, Z. Zhao, Z. Xie, Z. Sun, *Nanoscale* **2013**, *5*, 12272.